Residual stress reductions of carbide cutting tools through applying pulsed magnetic field and coupled electromagnetic field – mechanism analysis and comparison study

Fu Zhong[a], Jie Wang[a], Qianwen Zhang[a], Jigang Huang[a], Wei Wang[a], Jie Xu[b], Kunlan Huang[a,] *, Yi Qin[c,] *

[a] *School of Mechanical Engineering, Sichuan University, Chengdu, Sichuan 610065, P.R. China*

[b] *School of Materials Science and Engineering, Harbin Institute of Technology, Harbin 150001, P.R. China*

[c] *Centre for Precision Manufacturing, Dept. of Design, Manufacturing and Engineering Management, The University of Strathclyde, James Weir Building, 75 Montrose Street, Glasgow G1 1XJ, UK*

* Corresponding authors:

E-mail address: huangkunlan@scu.edu.cn (Kunlan Huang); qin.yi@strath.ac.uk (Yi Qin)

This is a peer-reviewed, accepted author manuscript of the following article: Zhong, F., Wang, J., Zhang, Q., Huang, J., Wang, W., Xu, J., Huang, K., & Qin, Y. (2022). Residual stress reductions of carbide cutting tools through applying pulsed magnetic field and coupled electromagnetic field – mechanism analysis and comparison study. The International Journal of Advanced Manufacturing Technology, 121(7-8), 4757–4775. https://doi.org/10.1007/s00170-022-09434-3

ABSTRACT

The residual stress reductions of metals enabled by external field treatments such as magnetic field and coupled electromagnetic field treatments are of high industrial significance. Their applications are, however, far from satisfactions, largely due to the mechanisms involving the residual stress reductions by those treatment methods are still not understood fully and hence, there still exist sophisticated issues regarding process reliability and design clarity, and more reliable and controllable treatment processes are still to be achieved.

In the present work, both pulsed magnetic treatment (PMT) and coupled electromagnetic treatment (ECT) were used to reduce the residual stress in P10 carbide tools. Besides residual stress measurements and microscopic observations of dislocations in the tested tools, a new model for modelling dislocation-interactions in the treated tools was developed. More complex mechanisms of the microstructural changes induced by the external fields were newly revealed. The microstructural changes are correlated quantitatively to the residual stress reductions in a greater detail. These efforts have resulted in new knowledges in the field of treating cutting tools by applying external fields.

The dislocation morphology observed with a Transmission Electron Microscope was examined on their characteristics, quantity, and distribution. It was suggested that the WC phase with the dislocation of multiple quantities and wide distribution could be obtained easily through the ECT.

Deformation displacements and directions, internal stresses and volume strains, calculated using a transient 3D model with COMSOL (Multiphysics software), were compared. It was revealed that only the linear magnetostriction effect occurred during the PMT, while the linear magnetostriction effect and the Weidemann effect both existed during the ECT.

Compared with the PMT, the internal stress and the volume strain induced by the ECT were remarkably higher. There was a mutation phenomenon of the stress magnitude and direction during the ECT.

Additionally, it was quantitatively confirmed that the internal stress produced during electromagnetic processing could force the dislocation to move. By studying the Frank-Read source and the characteristics of the stress obtained by simulation, it was inferred that the ECT was more conducive to the dislocation multiplication.

The proposed Opposite Sign Parallel Dislocation Interaction Model also showed that the interactions between dislocations could effectively reduce the lattice distortion at the severe distortion area of the dislocations.

The study showed that the residual compressive stress could be effectively reduced by the evenly enhanced dislocation stretching and compression asymmetry after dislocation multiplication. The results obtained with the X-ray diffraction method demonstrated a 30% stress reduction with the PMT and a 65% reduction with the ECT.

Keywords: Residual stress, Cutting tool, Pulsed magnetic field treatment (PMT),

Coupled electromagnetic treatment (ECT), Magnetostriction effect, Dislocation interaction

1. Introduction

The demands for higher machining accuracy and longer tool life have been increasing, resulting in many new challenges for improving tool quality and tool performance. Although P10 carbide tools have very impressive properties already, such as high-temperature resistance, excellent abrasion resistance, prominent hardness, etc [1,2]. There are still a lot of concerns about the tool life and tool-costs, particularly for semi-finishing and finishing machining, largely due to the number of tools used in industry is very high [3]. New solutions for further improving cutting-tool life are continuously being sought. Al-Ethari et al. [4] and Rech et al. [5] found that the lifetime of coated tools was about four times longer, compared to the uncoated tools. Liu et al. [6] developed a green processing method, which showed that the use of a mixture of water vapor and gas could reduce the main cutting force resulting in the tool life being much longer. At the same time, Yuan et al. [7,8] proposed a method using pulsed coupled electromagnetic field to process a WC-15TiC-6Co cermet tool to improve the tool life. This method could overcome some key limitations from a conventional treatment process which was usually tedious and would require complex equipment.

Electromagnetic treatment of metals has been applied in commercial sense ever since Vivès developed an electromagnetic processing method. Akram et al. [4] reported improvements in fatigue endurance, Vickers microhardness and tensile strength for both EN8 steel and AA2014-T6 alloy treated by an alternating magnetic field (0.54T). Gu et al. [9] found that after the treatment of a magnetic field, the fatigue life of a 35CrMo

steel was increased. Le et al. [10–13] studied the effects of an oscillating electromagnetic field on grain refinement and phase formation, indicating that the Lorentz force could result in a change of the cooling rate and a more uniform temperature distribution. Yang et al. [14,15] pointed out that the detouring of an eddy current around a fatigue crack caused the voltage breakdown and the transient thermal compressive stress which were main factors to lead to healing in the fatigue crack initiation zone and the crack tip zone.

Although both electric current treatment [16,17] and magnetic field treatment [18,19] have certain effects on the properties of the materials treated, extent of the effects was limited by applying one kind of the field alone. Liu et al. [20] presented an innovative approach to change the cemented carbides' microstructures in order to improve milling and mechanical performances by combining pulsed magnetic and pulsed current fields, and the experimental results demonstrated that the electromagnetic process tended to promote the dislocation density of the cemented carbides, finally strengthening the material property. Yuan et al. [7] investigated effects of a coupled electromagnetic field on the cutting-tool life for P10 carbide tools. It was reported that the coupled electromagnetic field could promote an increase of the cemented carbide tool life for which the magnetic intensity was a key parameter.

A large residual stress could be formed during sintering of cemented carbide [21,22], which is about 150 MPa to 200 MPa. Several scholars have found that a pulsed magnetic field and the process combining a pulsed magnetic field and a pulsed current could effectively reduce residual stress. Klamecki [23] stated that when the pulsed

magnetic treatment was used on lower initial stress level specimens, residual stress decreased by 4%-7% and by 8%-13% for higher initial stress level specimens. Tang et al. [24,25] reported that the residual stress was measured to reduce by 20%-40% in the welded specimen residual stress tests which also showed that the internal stress relaxation might mainly be caused by the magnetic vibration. Cai et al [26,27] researched the effects of the magnetostriction on residual stress relief with pulsed magnetic treatment and the results showed that there was a range of magnetic field intensity that was appropriate for decreasing residual stresses. Yan et al. [28] found that the density dislocation morphology and parallel dislocation of rolled sheet grains would increase after pulsed magnetic field processing, which suggested that the pulsed magnetic field could generate the Lorentz force to lead to basal slip and thereby to result in local plastic deformation. Shao et al. [29,30] determined that the mechanism of residual stress reduction of 20Cr2Ni4A under 1 T pulsed magnetic field processing included the improvement of the dislocation movement flexibility and the proliferation and entanglement of the dislocation structure. Cai and Huang [31,32] reported the effect of an apparent reduction of residual stress in steel samples using a combination of pulsed magnetic field and pulsed current leading to electro-magneto-plasticity.

However, the mechanisms of residual stress release by electromagnetism have only been explained qualitatively. Cai et al. [33] found that magnetostriction variations had a close association with changing of the state of the stress and were valuable for the optimization of the processing parameters and evaluation of stress relief. Hou et al. [31] revealed that at lower magnetic fields (for instance, 1.0 T and 1.3 T), the dislocation

density and compressive residual stress tended to reduce, while these would increase when higher magnetic fields were applied (for example, 2.0 T and 2.5 T).

It was evident that the mechanisms how these fields actually influence the material stress states quantitively were unclear. Thus, numerical modeling of the electromagnetic fields and mechanical fields was developed in order to develop better understanding of the residual stress reduction mechanisms [33–35], considering two treatment methods – coupled electromagnetic treatment and pulsed magnetic field treatment.

Zhao et al. [36] used experimental and numerical methods to compare the deformation law and the bending effect in pure Al during surface-pulsed magneto-oscillation. Yu et al. [37] found that during magnetic pulse hole flanging, the inertia which was derived from high-speed formation had significant effects on the radial tensile stress. These suggest combining numerical simulation and experimental investigation to be a useful method to examine the phenomena associated with external field treatments of materials [38,39], since the magnetostriction effect is hardly seen at the macro level.

Although numerical investigations of the phenomena associated with external field treatments of metals have been attempted, there were no clear reports bridging between the microstructural changes induced by the external fields and stress-state changes in the cutting tools, with clear quantitative descriptions of those interrelationships, which are crucial for process design and quality control, and for defining process' reliability. Achieving this could enhance the stakeholders' confidence

in the applications of these technologies tremendously. In the present work, both pulsed magnetic treatment (PMT) and coupled electromagnetic treatment (ECT) were used to reduce the residual stress in P10 carbide tools. Besides residual stress measurements and microscopic observations of dislocations, a new model for modelling dislocation-interactions in the treated tools was developed. More complex mechanisms of the microstructural changes induced by the external fields were newly revealed. The microstructural changes are correlated quantitatively to the residual stress reductions. These efforts have resulted in new knowledges in the field of treating cutting tools by applying external fields and hence, enhanced our scientific understandings. The results could help to promote the applications of these techniques more widely.

2. Experiment

In the study reported in this paper, two kinds of experiment - PMT and ECT of the tools, were performed, which were then followed by residual stress measurements and microstructural observations. For a purpose of comparison, the tool specimens were divided into three groups: tools that were not treated, and ones that were treated with the PMT and ECT respectively.

The tools that need to be treated with the PMT and ECT were firstly measured for their residual stresses, followed by performing the PMT and ECT respectively. After the tools were treated, these were measured again on their residual stress in situ. For the microstructural observation, both tools which were untreated and treated by the PMT and ECT were examined. Results of the residual stress measured and

microstructural observations were compared and analyzed for both treated and untreated cases as well as for the two different treatment techniques.

2.1. Experimental apparatus and tool samples

Fig. 1 (a) shows the experimental instrument used in this study. The experimental device consisted of a magnetic field system, current field system and shield protective system. The magnetic field system is comprised of an excitation coil with a pulse current that could generate a magnetic field from 0 T to 2 T. The current system provides the pulse ac square wave current and clamps the workpiece simultaneously. The clamping is achieved by one electrode fixed inside the working chamber. The other electrodes could be moved axially along the working chamber. The shield protective system is essential for the electromagnetic treatment equipment to be operated safely.

A P10 carbide tool was used as the study object for the pulsed magnetic field treatment and electromagnetic coupling treatment. The chemical composition of the P10 cemented carbide tool is 79% tungsten carbide, 15% titanium carbide, and 6% cobalt. Two samples were prepared for the residual stress detection. As is shown in Fig. 1 (b), the residual stress test and the microstructure observation were carried out at the flank surface, with an area of 0.3 mm×0.5 mm. X-ray diffraction was used to measure the residual stress before and after the treatment. Fig. 1 (b) shows the x and y directions. The x and y directions were both measured, and they were denoted as σ_x and σ_y.

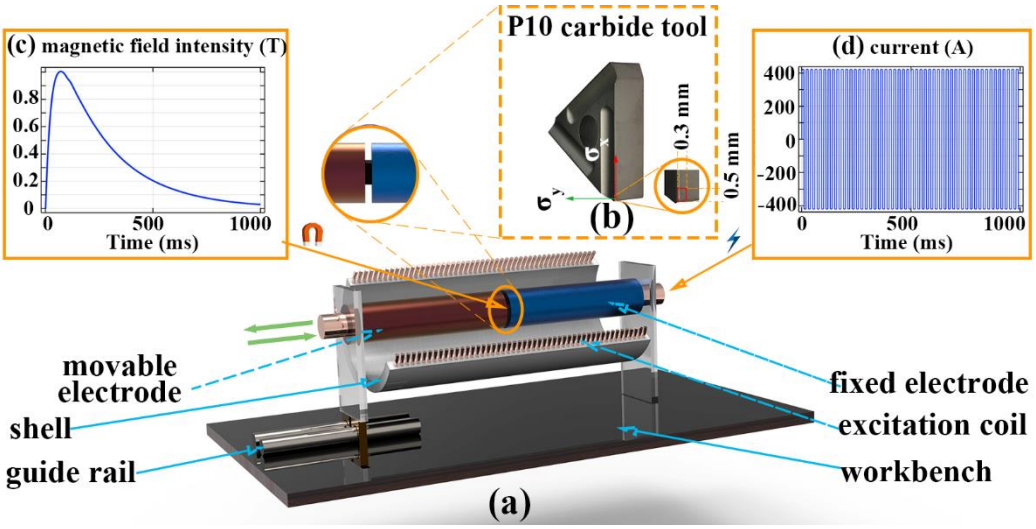

Fig. 1 Schematic of the experimental device for PMT and ECT and conditions of the magnetic field and electrode current: (a) Experimental apparatus; (b) P10 carbide tool; (c) Magnetic field intensity at the central symmetry of the coil axis; and (d) Electrode pulse ac square wave current.

2.2. Experimental procedure, parameters and methods

2.2.1. Procedure

Fig. 2 shows that the residual stress of the two samples was measured to obtain the initial residual stress value before the treatment. Then, the two samples were treated with the PMT and ECT and the residual stress was measured after the treatment. Finally, the effects on the residual stress reduction for the two treatment methods were compared. At the same time, three additional samples were prepared for microscopic observation to analyze the mechanisms of the residual stress reduction. One sample, without any treatment, was used for a blank control experiment. The other samples were also treated by the PMT and ECT. The microscopic observation was carried out with a

Transmission Electron Microscope. The microscopic observation was for examining dislocation morphology, and dislocation characteristics of the WC phase, TiC phase, and Co phase were compared.

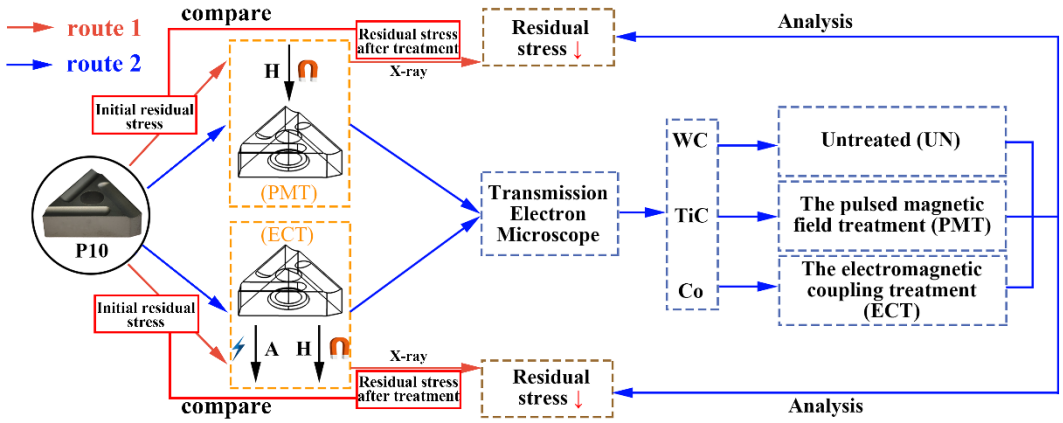

Fig. 2 Experimental procedure for residual stress detection (route 1) and microscopic observation (route 2).

2.2.2. Experimental parameters

Fig. 1 (c) shows that the magnetic field boundary condition with the peak magnetic field intensity of 1 T was finally determined by conducting the previous experiment. The pulse frequency of the magnetic field was about 1 Hz, and 25 pulses were used in total. Fig. 1 (d) shows the current waveform during the treatment. The peak value of current was near 420 A, and the duration of each pulse was 20ms. The electrode current lasted for 25 s.

2.2.3. Residual stress measurement

An X-ray equipment called Proto LXRD micro-area residual stress measuring system was used to measure the residual stresses in the tool samples. According to GB/T

7704-2017, the measurement was carried out with a double detector co-inclination method, including Cu target K_a radiation, Ni filter, 0.5 mm collimator, 11 beta angles, maximum beta angle of 35°, 212 crystal surface, exposure time of 4 s, and 15 times of exposures.

2.2.4. Sample preparation for microstructural observation

The specimens for the TEM (Transmission Electron Microscope) examinations were sampled at the flank surface of the cutters. Mechanical thinning followed by ion milling were used to prepare the specimens at room temperature. A diamond saw was used to cut the sintered samples into discs on an ultrasonic disc cutter. The disk was then polished using a precision ion beam thinning instrument (Gatan-695). A Transmission Electron Microscope (FEI Talos F200X) was used to observe the microstructures of the samples at 200 kV.

3. Experimental results

The residual stresses measured for both cases – tools treated by the two methods respectively and ones not treated, were obtained and are presented in this section. TEM and EDS results of the WC, TiC, and Co phases of the tools obtained for these cases are also presented here.

3.1. Residual stress and reduction

Table 1 lists the residual stress changes in the X and Y directions after the PMT

and ECT of the cutting tool samples. After the PMT, the average residual stresses of the X and Y directions decreased by about 30%. However, after the ECT, the average residual stresses along both the X and Y directions decreased significantly, e.g., by more than 65%. It was certain that using PMT and ECT the residual stress of the cutters could be reduced. Nevertheless, the ECT was more effective than PMT.

Table 1 Residual stress changes in the cutter samples due to the PMT and ECT.

	Direction	Before treatment $\boldsymbol{\sigma}$**(MPa)**	After treatment $\boldsymbol{\sigma'}$**(MPa)**	Residual stress changes $\boldsymbol{\lvert\sigma-\sigma'\rvert}$**(MPa)**	Relative changes (%) $\boldsymbol{\sigma-\sigma'/\sigma}$
PMT	σ_x	-132	-96	36	27.3
	σ_y	-164	-104	60	36.6
ECT	σ_x	-169	-54	115	68.0
	σ_y	-98	-34	64	65.3

3.2. Microstructure observation of dislocation

Fig. 3 shows the TEM light field image of the untreated P10 carbide tool. The object images of the corresponding morphologies at the selected area for energy spectrum analysis were for the WC phase, TiC phase and Co phase respectively.

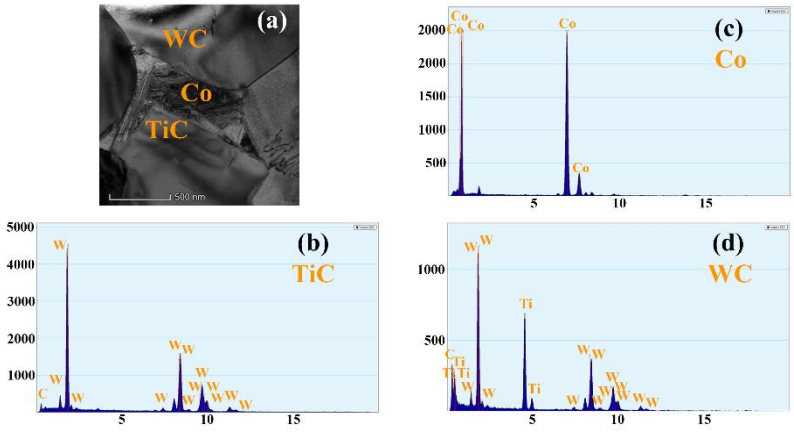

Fig. 3 Bright field image and energy spectrum of P10 carbide tool; EDS results (b-d) acquired in (a).

As illustrated in Fig. 4, the grain microstructures of the WC, TiC, and Co phases after different treatments confirm that the microstructure of the P10 carbide tool had been changed due to the electromagnetic treatment. Fig. 4 (a), Fig. 4 (e), and Fig. 4 (i), could be used to gain an overall understanding of the microstructure of the three phases after different treatments. The dislocation movements and the multiplication were more evident in the WC phase and the TiC phase. However, in the Co phase, there were mainly “stacking faults”.

Fig. 4 (b), Fig. 4 (f), and Fig. 4 (j) highlight the multiplication of dislocation in the WC phase. It can be observed from the figures that few dislocation lines appeared in the WC of the untreated sample. Compared with the untreated specimen, the dislocation density of the PMT specimen had a significant increase. However, the dislocation lines interconnected with each other, resulting in a dispersed dislocation network microstructure. Compared with Fig. 4 (b) and Fig. 4 (f), the dislocation morphology shown in Fig. 4 (j) was characterized by multiple quantities, a wide distribution, a network, and more homogenization.

Fig. 4 (c), Fig. 4 (g), and Fig. 4 (k) highlight the multiplication of dislocation in the TiC phase. In the untreated sample, there were few dislocations. After the PMT and ECT, a similar multiplication of dislocations was also observed in the TiC phase, as shown in Fig. 4 (g) and Fig. 4 (k). However, the dislocations in the TiC phase were less than those in the WC phase. The WC phase was generally affected by hardness.

Fig. 4 (d), Fig. 4 (h), and Fig. 4 (l) highlight the change of the stacking faults in the Co phase. It can be observed that obvious stacking faults with one direction occurred

in the Co phase of the untreated sample. After the PMT, the stacking faults became more dense with more directions.

Therefore, as observed with the microscopic structure, the electromagnetic processing technology can result in dislocation multiplication in the crystal. Additionally, the effect of the ECT was more obvious. It can be concluded that the dislocation multiplication after the PMT was inexhaustive and not obvious. After the ECT, the dislocation multiplication was exhaustive and obvious.

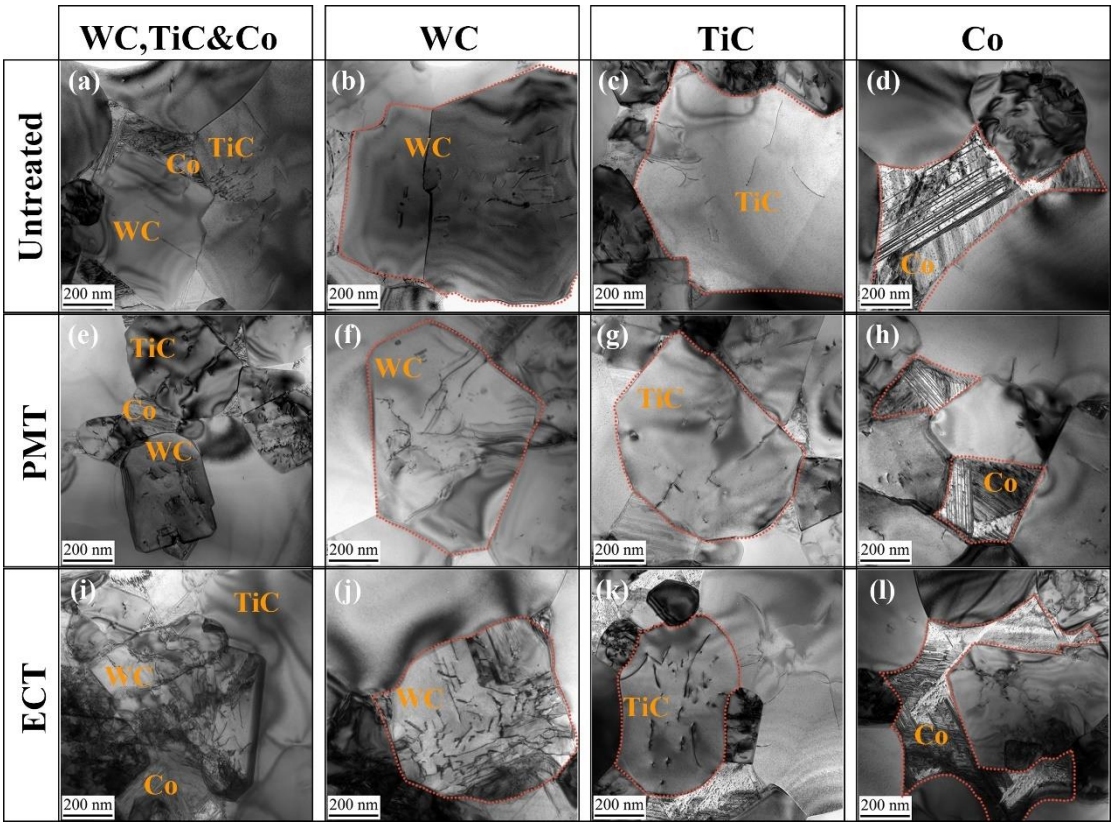

Fig. 4 Comparison of grain microstructures of the WC, TiC, and Co phases after different treatments and untreated phases. (a), (b), (c), and (d) Untreated; (e), (f), (g), and (h) After the PMT; (i), (j), (k), and (l) After the ECT.

4. Numerical simulation and result comparisons

This section presents the numeric simulation works which were undertaken with a view to assisting in developing further understanding of the mechanisms of the influences by the PMT and ECT processes on the residual stresses in the cutting tools. The simulations were carried out with COMSOL Multiphysics software. Results of the magnetostriction effects during the two treatments (PMT and ECT) were computed respectively and then compared. The deformation displacements and directions, internal stresses and volume strains were particularly compared.

4.1. Numeric modelling – model and procedure

Using the COMSOL Multiphysics to simultaneously solve the transient governing equations for the magnetic field, the electric field, and the structural mechanical field. First, the current curves were measured in the actual experiment, as shown in Fig. 1 (c) and (d). And then applying the software to set up the geometric model and boundary conditions. As shown in Fig. 5 (b), the 3D models were established with Solidworks, followed by the input of the Livelink interface in COMSOL Multiphysics. Fig. 5 (c) shows the finite element meshes. The P10 carbide tool, as the important study object, was divided into superfine mesh from 0.0811 mm to 2 mm. The other structures adopted a coarser meshing scheme to reduce the computational complexity. Fig. 5 (a) shows the numerical simulation procedure.

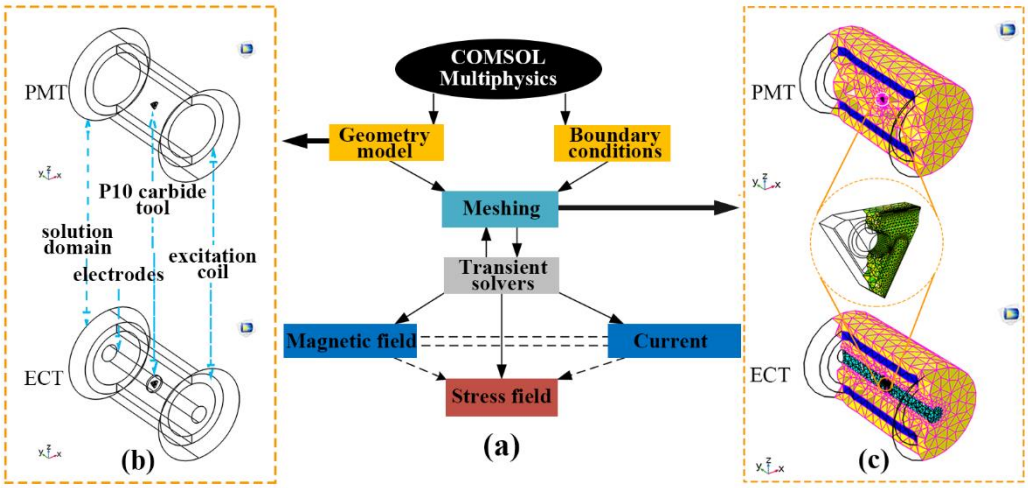

Fig. 5 Numerical models and simulation procddure: (a) Procedure of the numerical simulation with COMSOL Multiphysics software; (b) Geometry models; (c) Mesh for analysis.

4.2. Comparison of simulation results

4.2.1. Magnetostriction effect in PMT and ECT

The magnetostriction effect was investigated to analyze the physical phenomena of the ferromagnetic material of the P10 carbide tool during the applied electromagnetic field treatment. The reason that the results from 100ms to 144ms were selected was that the deformation of the tool during this period changes from a weak state to a strong state and then to the weak state again. In the P10 carbide tool, the displacement of one edge (named “mn”) that was parallel to the main magnetic field was separately examined. The differences for the magnetostriction effect between the PMT and ECT were compared.

During the PMT, there was only the linear magnetostriction effect so that the

maximum deformation displacement was 96 nm, as shown in Fig. 6 and Fig. 7. Moreover, it was clear that the displacement component at the boundary in the X direction was about 5 nm, in a single and stable direction, being caused by the induced current.

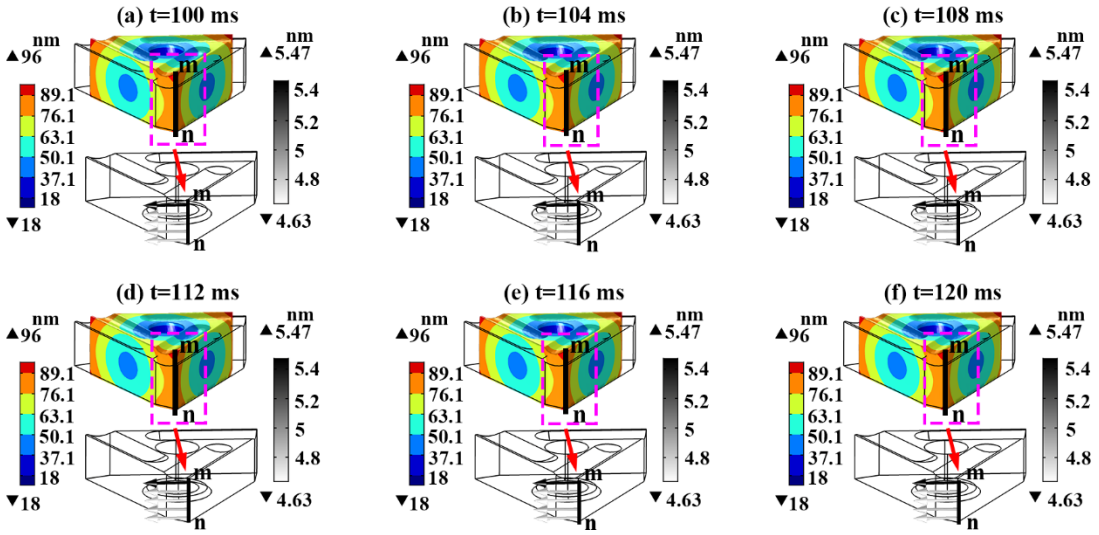

Fig. 6 The deformation of a tool from 100 ms to 120 ms during PMT: (a) t=100ms; (b) t=104ms; (c) t=108ms; (d) t=112ms; (e) t=116ms; and (f) t=120ms. The overall deformation: the solid black lines illustrate the initial state of the tool, and the part with colour shows the state of the tool deformation. The displacement components of the boundary “mn”: the color legend shows the deformation displacement, and the arrow represents the displacement direction and magnitude of “mn”.

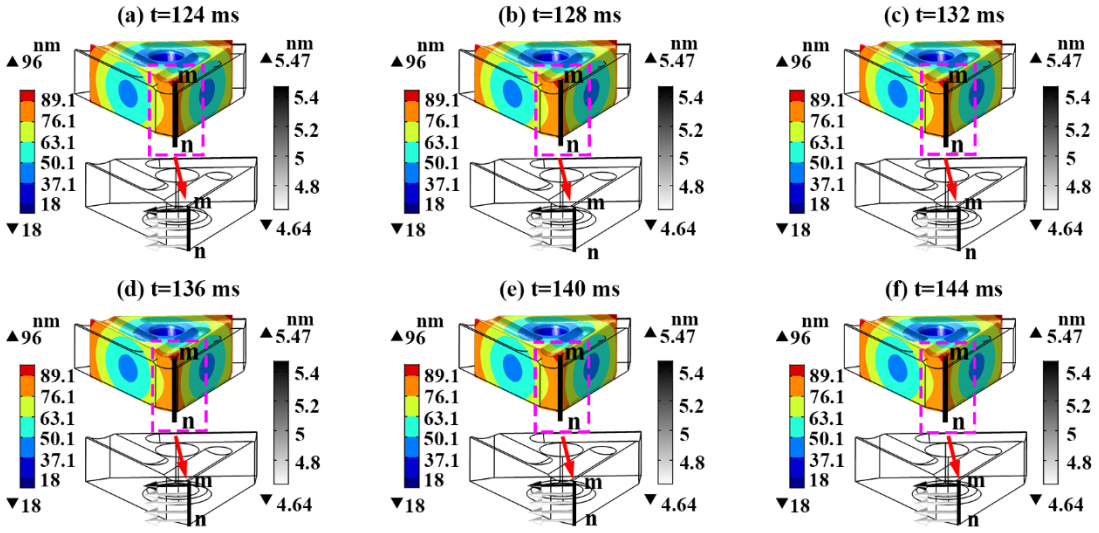

Fig. 7 The deformation of a tool from 124 ms to 144 ms during PMT: (a) t=124ms; (b) t=128ms; (c) t=132ms; (d) t=136ms; (e) t=140ms; and (f) t=144ms. The overall deformation: the solid black lines illustrate the initial state of the tool, and the part with color shows the state of the tool deformation. The displacement components of the boundary "mn": the color legend shows the deformation displacement and the arrow represents the displacement direction and magnitude of "mn".

During the ECT, it was interesting to note that there was not only linear magnetostriction, but also the Wiedemann effect, as shown in Fig. 8 and Fig. 9. The maximum displacement also was 96 nm. However, it was notable that the displacement component of boundary "mn" in the X direction was near 90 nm, which was about 18 times that from the PMT. Moreover, the direction of the displacement at point "m" and point "n" was opposite and changing. The closer the location was to point "m" and point "n", the greater the displacement was. In the electromagnetic coupling treatment process, the P10 carbide tool had telescopic deformation and torsional deformation.

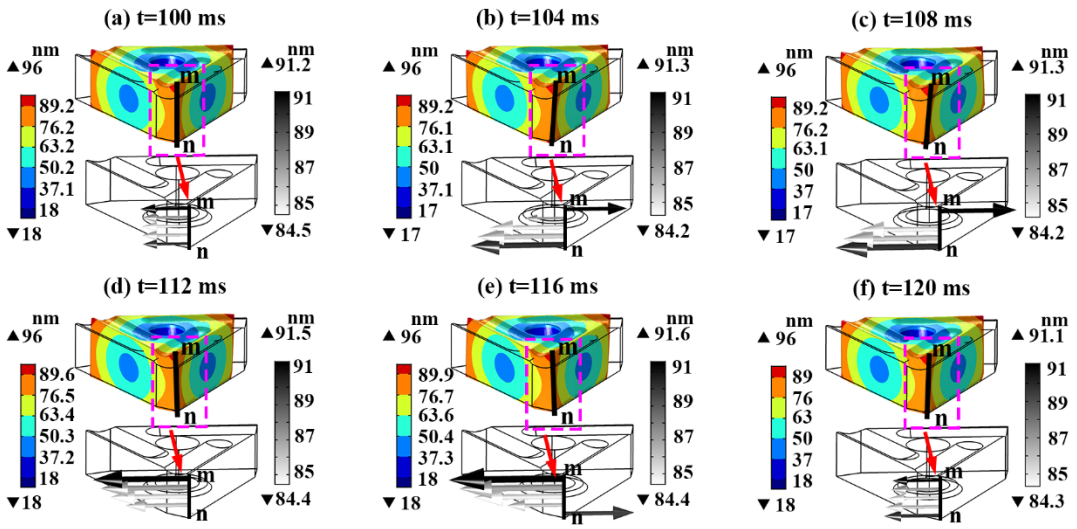

Fig. 8 The deformation of a tool from 100 ms to 120 ms during ECT: (a) t=100ms; (b) t=104ms; (c) t=108ms; (d) t=112ms; (e) t=116ms; and (f) t=120ms. The overall deformation: the solid black lines illustrate the initial state of the tool, and the part with colour shows the state of the tool deformation. The displacement components of the boundary "mn": the color legend shows the deformation displacement, and the arrow represents the displacement direction and magnitude of "mn".

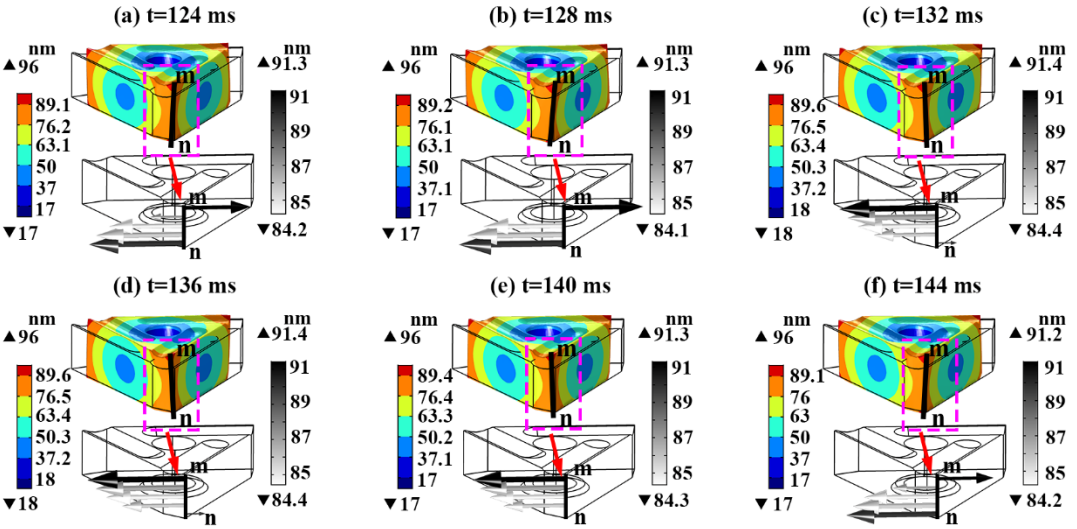

Fig. 9 The deformation of a tool from 124 ms to 144 ms during ECT: (a) t=124ms; (b) t=128ms; (c) t=132ms; (d) t=136ms; (e) t=140ms; and (f) t=144ms. The overall deformation: the solid black lines illustrate the initial state of the tool, and the part with

colour show the state of the tool deformation. The displacement components of the boundary “mn”: the color legend shows the deformation displacement, and the arrow represented the displacement direction and magnitude of “mn”.

As shown from Fig. (6) to Fig. (9), the tool deformations occurred in the main magnetic field direction where the tool dimension was extended as well as in the plane of the upper surface of the cutter where the tool dimension contracted inwards. Finally, the linear magnetostriction effect that occurred during the PMT was defined as stable and gentle. The linear magnetostriction effect and the Wiedemann effect that occurred during ECT were defined as twisting and changing.

4.2.2. Displacement curl

A pulse current cycle was selected to study the displacement direction and magnitude at any position inside the tool. The displacement curl can better describe the displacement state of a point in the three-dimensional field, as shown in Fig. 10 and Fig. 11. It was notable that in the coupled electromagnetic treatment, the internal deformation and the displacement of the P10 carbide tool were complex and multidirectional, and they changed periodically.

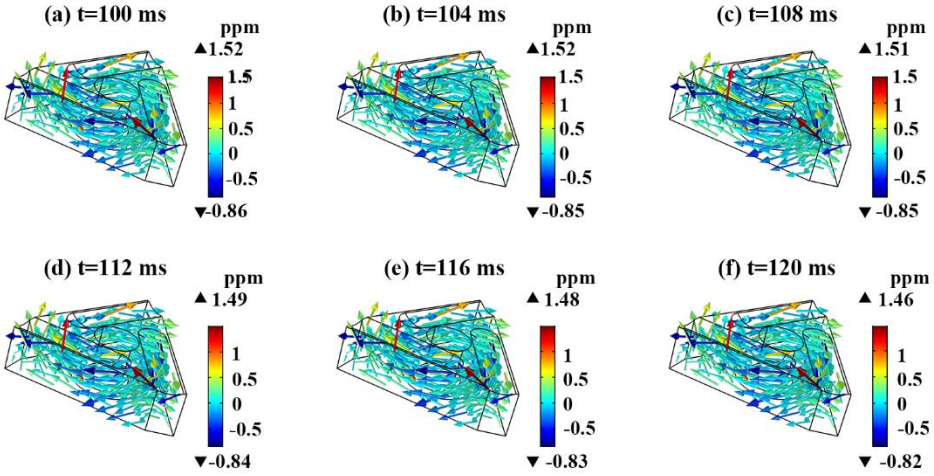

Fig. 10 Displacement curl of a tool during PMT from 100 ms to 120 ms: (a) t=100ms; (b) t=104ms; (c) t=108ms; (d) t=112ms; (e) t=116ms; and (f) t=120ms. The direction of arrows represented the direction of displacement curl, and the color legend represented the magnitude of displacement curl.

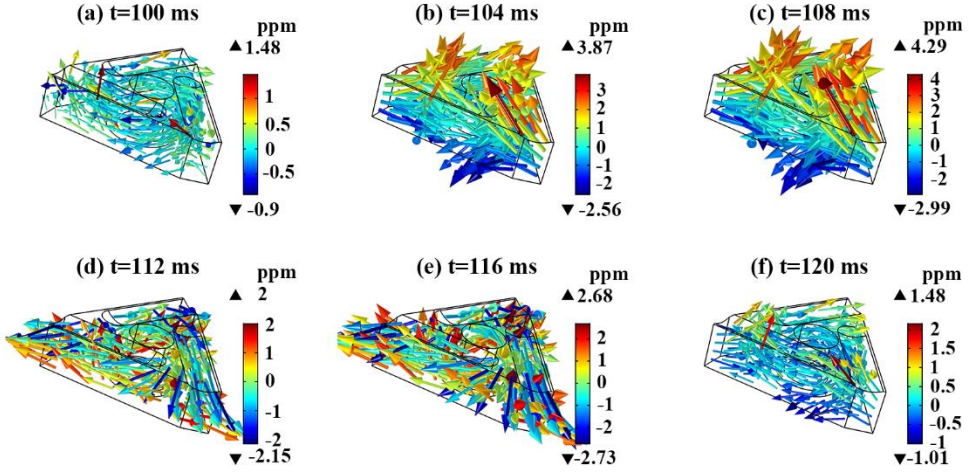

Fig. 11 Displacement curl of a tool during ECT from 100 ms to 120 ms: (a) t=100ms; (b) t=104ms; (c) t=108ms; (d) t=112ms; (e) t=116ms; and (f) t=120ms. The direction of arrows represented the direction of displacement curl, and the color legend represented the magnitude of displacement curl.

4.2.3. Strain-stress field

The deformation displacement during the magnetostriction effect inevitably generated a stress field inside the P10 carbide tool. As shown in Fig. 12 (a), it was clear that the average stress variation trend was similar for both PMT and ECT. However, there were two significant differences. One difference was that the average stress of ECT was twice that of PMT. The other difference was that the average stress generated in PMT was gentle, while the average stress generated in ECT was oscillatory and mutational. The average stress was nearly 10^5 Pa for both PMT and ECT. Fig. 12 (b) shows the maximum stress of the P10 carbide tool during the PMT and ECT. In the PMT, the maximum stress was about $3.4 \times 10^6\ Pa$, while in ECT, the maximum stress was about $4.0 \times 10^6\ Pa$.

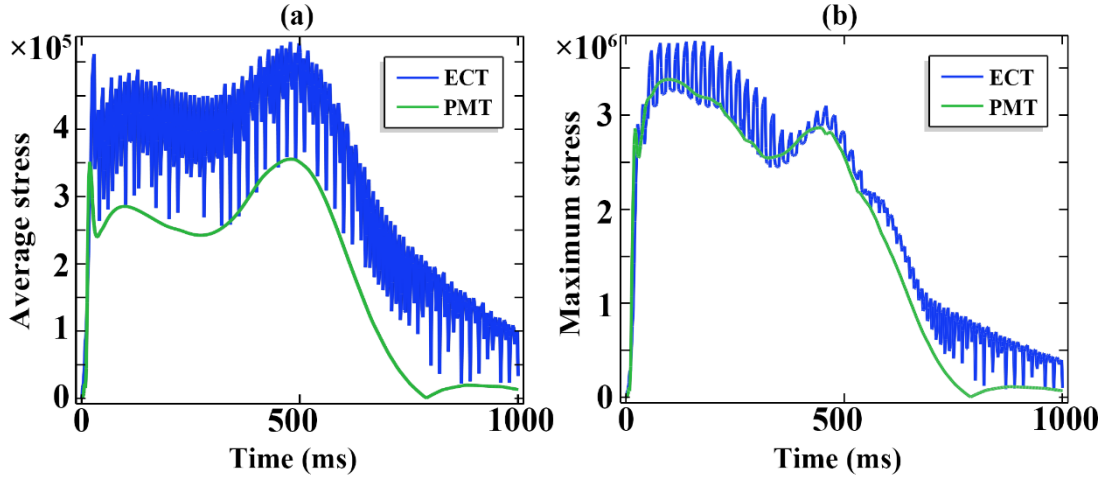

Fig. 12 Average stress and maximum stress of a P10 carbide tool during PMT and ECT: (a) average stress; and (b) maximum stress.

Fig. 13 shows the direction of the stress for PMT and ECT from 100 ms to 120 ms. The stress generated during PMT had a stable direction. However, the stress in ECT could be described as variable in direction. Therefore, it could be determined that the stresses produced in the two different processes were very different, with distinctions

in terms of the magnitude and characteristics.

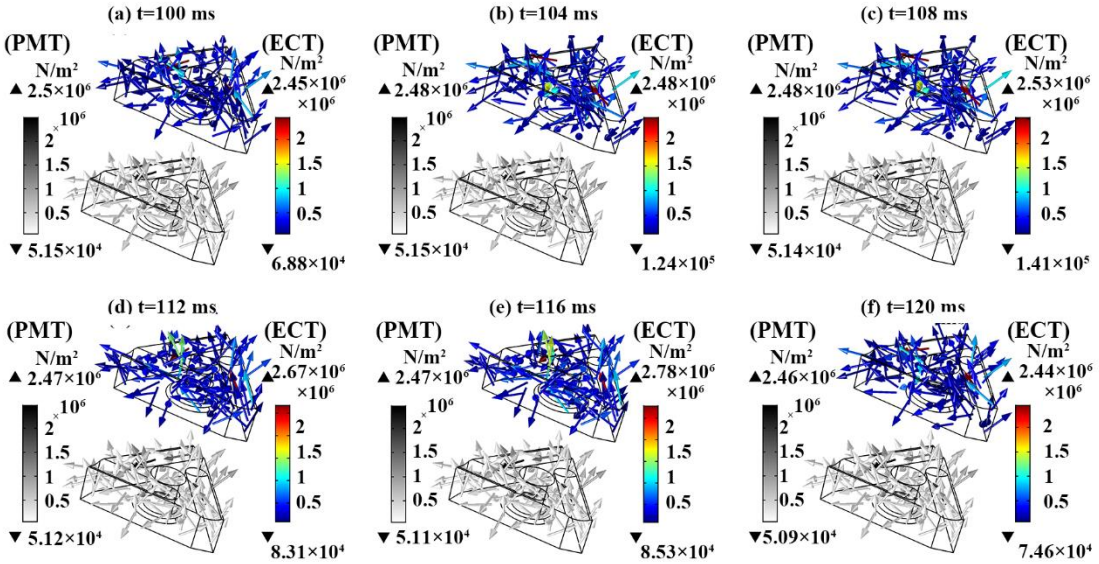

Fig. 13 Directions of the stress in tools during the PMT and ECT respectively from 100 ms to 120 ms: (a) t=100ms; (b) t=104ms; (c) t=108ms; (d) t=112ms; (e) t=116ms; and (f) t=120ms.

Volume strain was a good parameter for describing the change in volume at a particular location. Fig. 14 (a) shows that two boundary points and one internal point for a P10 carbide tool were selected to compare the volume strain. Fig. 14 (b) shows the volume strain for the PMT. It was notable that the volume strain at point 1 changed the most, which meant that the volume of the tip changed dramatically. The change of the volume strain at point 3 was the smallest, which meant that the change of the volume inside the tool was gentler. Moreover, volume extension and contraction occurred at three test points, while volume extension mainly occurred at points 1 and 2. Fig. 14 (c) shows the volume strain for ECT. There was volume mutation during ECT, for which the most obvious difference was the volume strain between PMT and ECT. There was an increase in the time of volume contraction of point 1 and point 2. Based on Fig. 14

(d), the variation trend of the volume strain in ECT was like that in PMT.

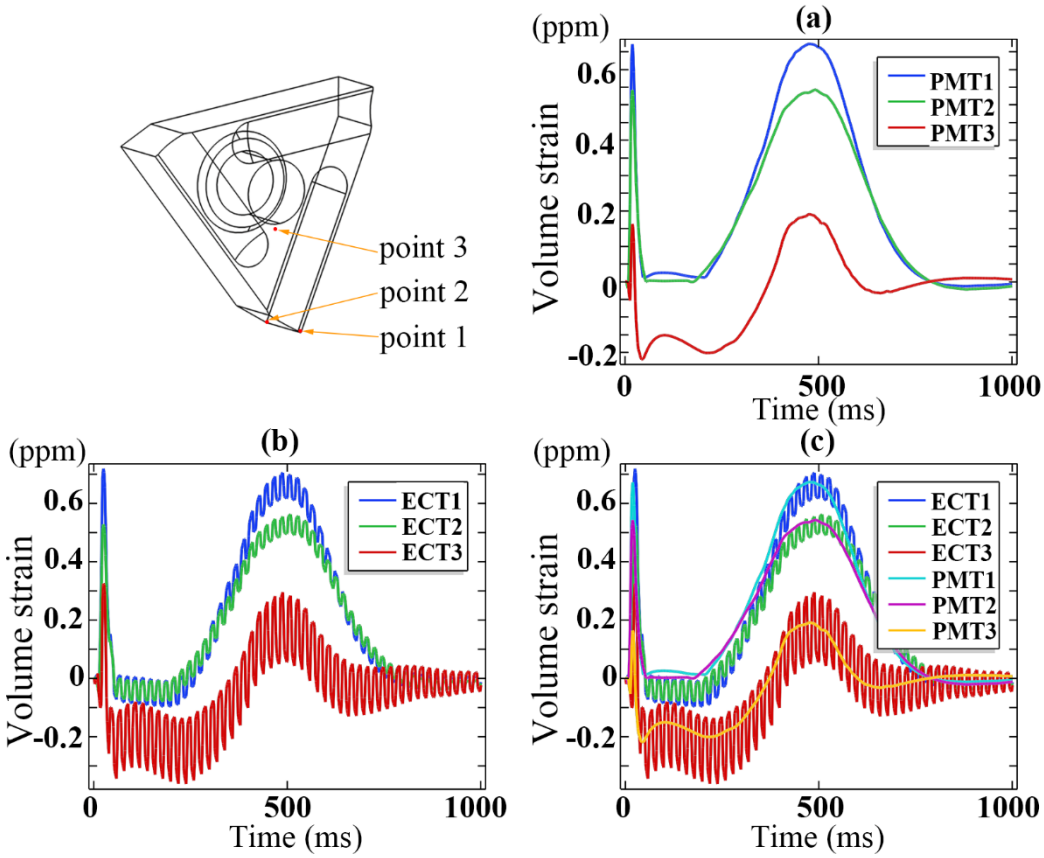

Fig. 14 Volume strain of the test points: (a) Three test points for volume strain of tools; (b) Volume strain of test points during PMT; (c) Volume strain of test points during ECT; and (d) Volume strain contrast between PMT and ECT.

5. Discussion

The simulation results indicated that the linear magnetostriction effect and Weidemann effect are significant for the treated tools, and their causes are discussed in this section. While the internal stresses induced by the magnetostriction effect seem having played a significant role in influencing the residual stress changes, how such stresses drive dislocations movement in the tools are also discussed. A model named as Opposite Sign Parallel Dislocation Interaction Model (OSPDIM) is also proposed for

aiding understanding on the reduction of the lattice distortion in the region having severe dislocation deformations, induced by the interactions after the dislocation movements. Combining with the Lanner-Jones potential function, residual stress reductions as well as reduction of the dislocation damages due to dislocation multiplications and interactions are also analysed.

5.1. The linear magnetostriction effect and Weidemann effect

During the PMT, the main extension direction of the P10 carbide tool was parallel to the main magnetic field direction, this was the linear magnetostriction effect. However, during the ECT, it was clear that torsional strain also existed during the deformation of the P10 carbide tool, and this was due to the Weidemann effect.

Through the external magnetic field action, the chain lengths of the metal atoms were changed, which resulted in a change of the domain volume [40,41]. Fig. 15 (a) and Fig. 15 (b) show the strain state of the domain after the addition of the external magnetic field. Fig. 15 (b) shows the external magnetic field applied along the direction of the arrow labeled as H. The shrink and the growth of the domains were achieved by the displacement of the domain walls. This displacement would directly lead to the change of the stress field inside the tool [42].

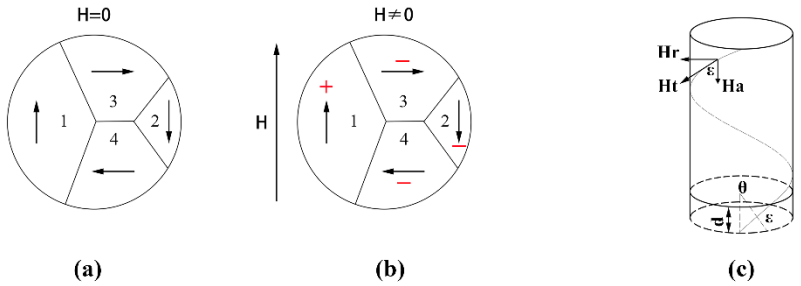

Fig. 15 (a) The domain state without a magnetic field; (b) The domain changes of the linear magnetostriction effect under a magnetic field "H" [43]; (c) Rotating magnetic field "H_t" generated under the superposition of the annular "H_a" and the axial magnetic field "H_r" of the Weidemann effect [44].

As shown in Fig. 15 (c), the essence of the Weidemann effect was that a torsional magnetic field would be generated under the superposition of the annular and the axial magnetic field [42], and the torsional strain occurred for the domain structure under the torsional magnetic field action. The domain structure of the tool changed along the torsional magnetic field, resulting in torsional strain subjected to the torsional magnetic field. Therefore, the P10 carbide tool was constantly stretched and twisted, which was a biggest difference from the PMT. Deng et al. [45,46] found that magnetostriction was an important factor for the Wiedemann effect and that the Wiedemann torsion increased with magnetostriction. Therefore, it was reasonable to believe that in the ECT, the effects of the current and the magnetic field were complementary.

5.2. Dislocation movement and multiplication under the action of the magnetostriction effect

The deformation caused by the magnetostriction effect will inevitably cause the internal stress of a P10 carbide tool. In this research, by comparing the stress obtained by simulation and the critical shear stress (Peierls stress) calculated with the Peierls-Nabarro (P-N) model, it was quantitatively confirmed that the internal stress produced during electromagnetic processing could drive the dislocation to move.

Firstly, the Peierls stress could be calculated by Eqs. (1) and (2) from Nabarro [47], and the parameters could be obtained from Table 2. Therefore, the critical shear stress required for dislocation movement in different grains could be calculated, as shown in Table 3. Secondly, as shown in Fig. 12, the average stress of the PMT and ECT was about $10^5\ Pa$. The maximum stress was about $10^6\ Pa$. Finally, it was necessary to compare the Peierls stress and the stress obtained by simulation. When the driving force was greater than the Peierls stress, dislocation movement would occur. However, because the critical shear stress was the result of a series of simplified problems, it was not perfect quantitatively. Lu et al [48,49] examined the classic Peierls theory of the dislocation and showed that the critical shear stress calculated with the P-N model was higher than the real critical shear stress (about one order of magnitude). Therefore, for the case of ignoring the error, it was considered that the stress ($\times 10^6$) had reached the critical shear stress ($\times 10^7$) of the dislocation movement.

$$\tau_P = \frac{2G}{1-\mu} e^{-\frac{2\pi c}{a(1-\mu)}}, \quad (1)$$

$$G = \frac{\mathrm{E}}{2(1+\mu)}. \quad (2)$$

Table 2

P10 carbide tool parameters.

E	**G**	$\boldsymbol{\mu}$
$\mathbf{520}\ \boldsymbol{GPa}$	$200\ GPa$	0.3

Table 3

Critical shear stress of different grains.

	WC	TiC	Co
Crystal structure	hex	fcc	fcc
Lattice constant (c: a)	0.9763	1	1
Peierls stress	8.936×10^7 Pa	7.223×10^7 Pa	7.223×10^7 Pa

Dislocations would proliferate in the process of dislocation movement. According to the multiplication mechanism of Frank-Read, dislocation multiplication occurred under the action of the simple force F [50]. The driving force of the dislocation played a crucial role in the dislocation movement and multiplication [51]. Combined with the analysis of Fig. 12, it could be inferred that the dislocation movement and the multiplication in the PMT were not inexhaustive and the multiplication effect was not obvious. In the ECT, the dislocation movement and the multiplication were more exhaustive and the multiplication effect was obvious. This inference was consistent with the dislocation morphology observed with the TEM, as shown in the Fig.4.

5.3. Mechanism of dislocation interaction

The previous section (*5.2*) described the proof that the electromagnetic treatment process could drive the dislocation movement and multiplication in the P10 carbide tool. The mechanism of dislocation interaction on the dislocation destructiveness reduction

and lattice distortion relief in the region with severe dislocation deformation was studied using the Opposite Sign Parallel Dislocation Interaction Model (OSPDIM).

5.3.1 Dislocation interaction

Schulz et al. [52,53] focused on discrete dislocations movement and the interaction between dislocations. Any dislocation in the crystal would generate a special stress field. Therefore, when two dislocations were close to a certain distance and the dislocations reached the range of their stress fields, the dislocations would appear to interact with each other [54].

In this study, edge dislocation was selected as an example to study the interactions between the two edge dislocations. As shown in Fig. 16 (a), F_x is the slip force that caused the dislocation e_2 to slip along the X-axis, F_y is the climbing force that enabled the dislocation e_2 to climb along the Y-axis. Fig. 16 (b) and Fig. 16 (c) detail F_x between the two dislocations. However, the climbing always corresponded to $F_y > 0$ in two opposite sign dislocations. The climbing always corresponded to $F_y < 0$ in two relative sign dislocations. As shown in Fig. 16 (b) and Fig. 16 (c), the relative positions of the two dislocations determined the direction of slip force and climbing force between the dislocations.

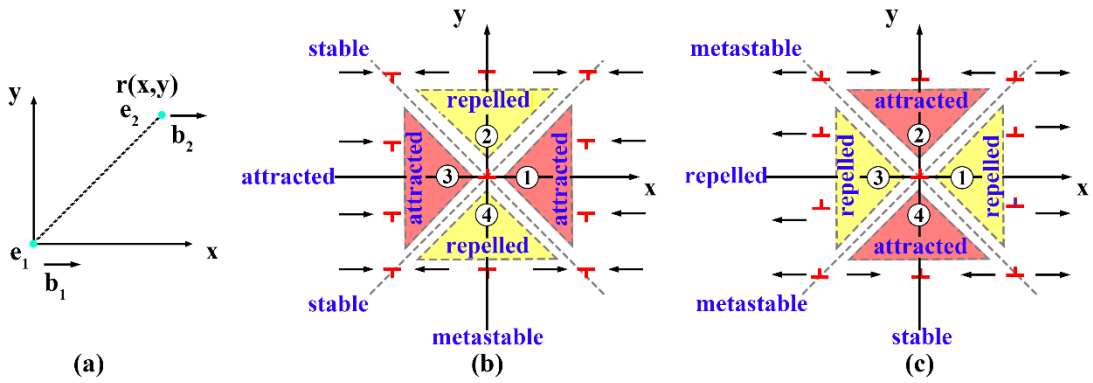

Fig. 16 The interaction of the two edge dislocations in the X-axis direction [55]. (a) Two edge dislocations, named e_1 and e_2, that were parallel with the Z-axes, were apart from r (x, y); (b) the relationship between the slip force and the position of two opposite sign dislocations; and (c) the relationship between the slip force and the position of the two relative sign dislocations.

Fig. 16(b) suggests that when e_2 laid at the interval of 1 and 3, the two dislocations attracted each other. When e_2 laid at the interval of 2 and 4, the two dislocations repelled each other. When e_2 was at $|x| = |y|$, two dislocations sat in a stable equilibrium position. When $x = 0$, e_2 was in the metastable state. When $y = 0$, e_2 and e_1 showed a mutual attraction; (c) The relationship between the slip force and the position of the two relative sign dislocations.

Fig. 16(c) indicates that the interaction forces between the two relative sign dislocations in the directions of F_x and F_y were opposite to those corresponding to the two opposite sign dislocations. The stable position and the metastable state of e_2 were just opposite to each other.

5.3.2 Opposite Sign Parallel Dislocation Interaction Model (OSPDIM)

The interaction of the two opposite sign parallel dislocations was analyzed based on the proposed Opposite Sign Parallel Dislocation Interaction Model, as shown in Fig. 17. Fig. 17 (a) shows the spacing between atoms 1 and 4 was stretched to the maximum. According to the Lennard-Jones potential, it was easy for the chemical bonds to break, resulting in plastic deformation, which was the biggest destructiveness of the dislocation that affected the fatigue life of the material [56].

As shown in Fig. 18 (a), each atom in the x direction was in a balance of shear stress and elastic stress, which was formulated as follows (Eq. (3)).

$$F_e = \sigma_s. \tag{3}$$

Schouwenaars et al. [57,58] determined the position of stress balance of all dislocations, and Qi et al. [59] determined that the motion of dislocation pairs could release the distortion energy stored, thus making the system more stable. Therefore, for the interaction between dislocations, it was thought that the dislocations had a specific arrangement that minimized the distortion energy.

As shown in Fig. 17 (b), two opposite and parallel dislocations attracted each other which maintained the equilibrium. As shown in Fig. 17 (c), when dislocation II approached dislocation I, the sliding force broke the balance between the original stress and the elastic stress, resulting in the atoms to be rearranged [44]. When dislocation I was fixed to the origin of coordinates but dislocation II was not fixed, the slip force of dislocation II was to the left on the macro level. However, dislocation I and dislocation II were characterized by mutual attraction and mutual force. Two

opposition sign parallel dislocations were bounded by the slip plane. The stress and the displacement of the upper and lower parts were similar. The slip force of the middle atoms in layer C between dislocation I and dislocation II was to the left, while that of the atoms in layer B was to the right, as shown in Fig. 17 (c). This caused the atoms in layer B to slip a certain distance to the left, and it caused the atoms in layer C to slip a certain distance to the right. The displacement between atoms 1 and 4 was showed in Fig 17 (d*). The* Δx was the displacement of the atom 4 on the X-axis influenced by dislocation II. Because the atom 4 was further away from the dislocation II than the atom 1 was, the atom 4 was less affected, as shown in Eqs. (5). Eqs. (4), (5), and (6) proved that the interaction between dislocations could effectively reduce the lattice distortion at a severe distortion area of the dislocations.

$$|n| > |\Delta x|, \tag{4}$$

$$n - \Delta x > 0, \tag{5}$$

$$l'_{14} = l_{14} - (n - \Delta x) < l_{14}. \tag{6}$$

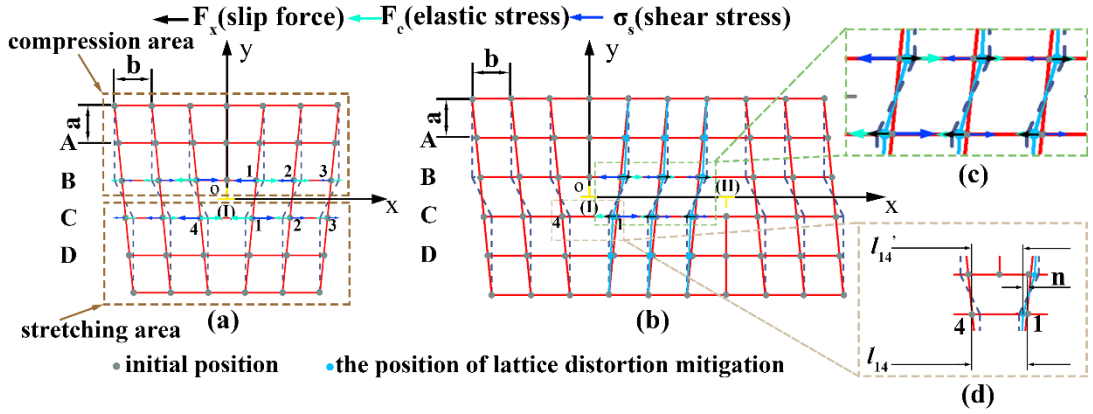

Fig. 17 The Opposite Sign Parallel Dislocation Interaction Model (OSPDIM). (a) A stable edge dislocation; (b) two interacting stable edge dislocations; (c) the direction of F_x, F_e, and σ_s; (d) the displacement description between atoms 1 and 4. l_{14} is the

spacing between atoms 1 and 4 in one edge dislocation. l'_{14} is the spacing between atoms 1 and 4 in OSPDIM. n is the displacement of the atom 1 on the X-axis, influenced by the dislocation II, which was no the left.

Shi et al. [60,61] suggested that the interactions between the atoms satisfied the rule of Lennard-Jones potential and the force law, based on the study of dislocation movements. Fig. 18 shows that in one edge dislocation model, when the applied external stress was F_a (the plastic stress was F_e), one pair of atoms were likely to break through the maximum elastic stress F_{max}. When two opposite sign parallel dislocations interacted, the stretching distance between atoms 1 and 4 was effectively reduced so that F_e was also reduced to F'_e. Therefore, there was a significant increase from F_a to F'_a in the endurance capacity of the external stress between atoms 1 and 4.

Finally, it could be concluded that the interaction between multiple dislocations could effectively reduce the lattice distortion in the region with severe dislocation deformation. Thus, the destructiveness of the dislocation was reduced and the endurance capacity of external stress was improved.

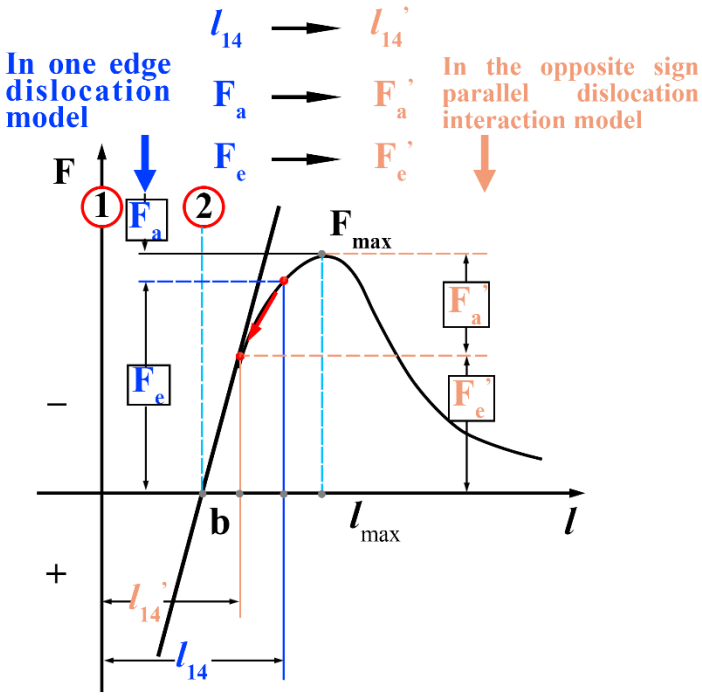

Fig. 18 The relationship between the displacement and force of the atoms based on the Lennard-Jones potential function. F_{max} and F'_{max} is the maximum elastic stress, F_a and F'_a the applied external stress, F_e and F'_e the plastic stress, l_{14} the spacing between the atoms 1 and 4 in one edge dislocation, and l'_{14} the spacing between the atoms 1 and 4 in OSPDIM.

5.3.3 Analysis of dislocation interaction in crystal

In order to verify the interaction between dislocations in crystal, a Fourier transform and an inverse Fourier transform were performed on the figures observed by HRTEM (High Resolution Transmission Electron Microscopy) to obtain the distribution and the direction of dislocation to verify OSPDIM, as shown in Fig. 19.

Fig. 4 (b) and Fig. 4 (c) showed that there were few dislocations in the WC phase

and the TiC phase in the untreated sample and the dislocations were lesser in Fig. 19 (b) and Fig. 19 (h). The dislocation interaction was difficult to find. Based on the one dislocation model, the distortion in the dislocation center was very serious. Thus, this kind of dislocation was a disadvantage with destructiveness for the material.

However, after the PMT and ECT, the distribution and direction of dislocation of the WC and TiC phases changed. As shown in Fig. 19 (d) and Fig. 19 (j), the dislocations were distributed in the state of interaction. For example, two or more dislocations were dislocated centrally. It was rare for one dislocation to exist. Two descriptions were defined to describe the state of dislocation. One description was mutual attraction: the slip force and the climbing force both pointed toward each other. The other description was non-mutual attraction: the sliding force and climbing force were not all pointing at each other. As shown in Fig. 19 (d), the dislocations in group (I) had non-mutual attraction and the dislocations in group (II) and (III) had mutual attraction. As shown in Fig. 19 (j), the dislocations in group (I) and (II) had mutual attraction. However, in group (III), the dislocations had non-mutual attraction and group (IV) had a metastable state. The climbing force in group (II) was the opposite. The slip force in group (III) was the opposite.

After the PMT, the interaction between dislocations was characterized by mutual attraction and non-mutual attraction. After the ECT, most of dislocation groups reached a more stable position of a steady state and a metastable state. Few groups had mutual attraction and non-mutual attraction, as shown in Fig. 19 (c) and Fig. 19 (f).

The interaction of dislocations can strengthen the properties of materials [42].

Based on the above observation, there were two levels of dislocation interaction after the PMT and ECT [62]. One was a lower level of mutual attraction and non-mutual attraction; the other was a deeper level of a steady state and a metastable state, which corresponded to the characteristics of the stress and the effect of dislocation multiplication in two different electromagnetic processes. Therefore, it could be concluded that after the PMT or ECT, the dislocations tended to interact. Additionally, after the ECT, the interaction of the dislocations was more stable.

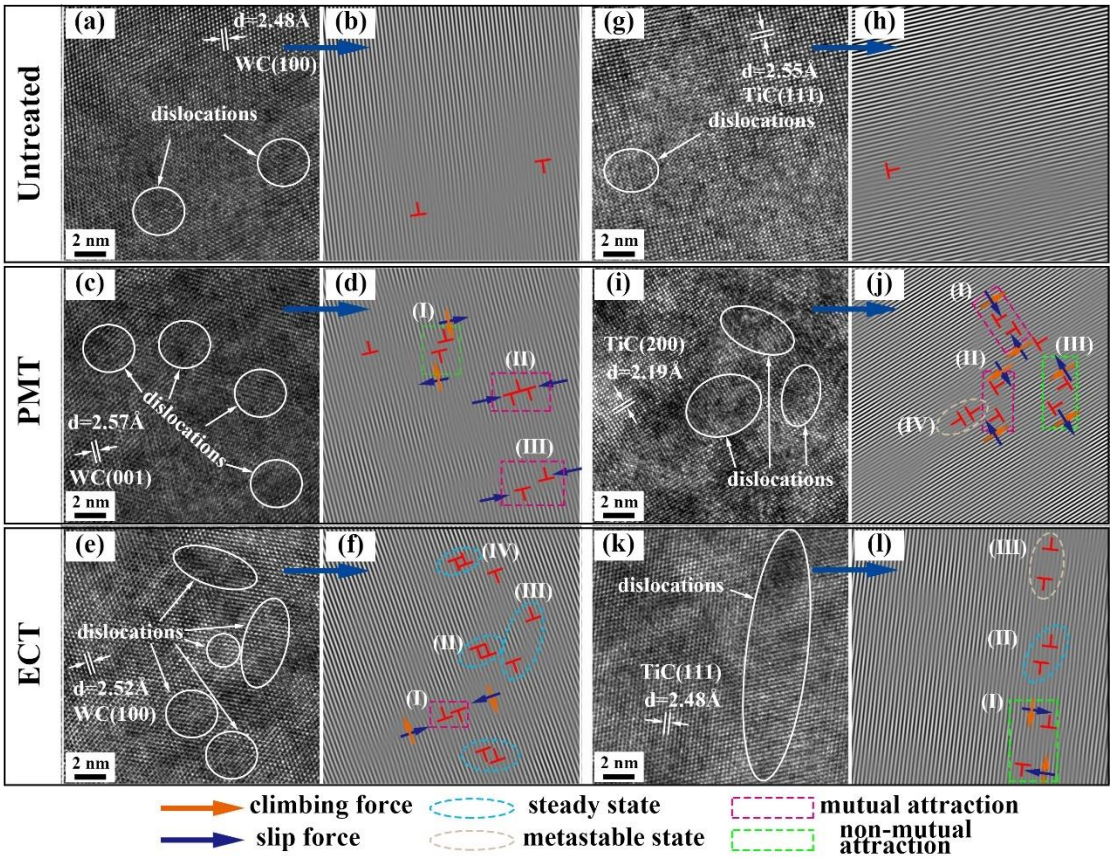

Fig. 19 The interaction of dislocations and the direction of dislocation interaction: (a) and (g) are WC and TiC phases of the untreated tools, respectively. (c) and (i) are WC and TiC phases after PMT, respectively. (e) and (k) are WC and TiC phases after ECT, respectively. (b), (h), (d), (j), (f), and (l) acquired from (a), (g), (c), (i), (e), and (k) respectively, by the Fourier transform and the inverse Fourier transform. Steady state:

two opposite dislocations are at $|x| = |y|$, or two parallel dislocations are at $x = 0$, as shown in Fig. 16. Metastable state: two opposite dislocations are at $x = 0$, or two parallel dislocations are at $|x| = |y|$, as shown in Fig. 16. Mutual attraction: the slip force and the climbing force both point towards each other. Non-mutual attraction: the sliding force and climbing force are not all pointing towards each other.

5.4. Mechanism of the residual stress change

Edge dislocation was selected as an example to study distortion. For one dislocation, there had to be a compression area and a stretching area when the slip plane was the boundary, as shown in Fig. 17 (a).

Dong et al. [63] determined that in terms of tension and compression, the dislocation nucleation mechanism had nothing in common. And the Lennard-Jones potential was used to study the stretching and compression area of dislocations in a crystal. According to Lennard-Jones potential, the force exerted on an atom is F, as shown in Eq. (7) [64]. Lim [65] quantitatively accounted for the differences in compression and stretching between atoms. Repulsive forces are more sensitive to changes in distance when the indices are such that $n < m$.

$$F(r) = -\frac{dU(r)}{dr} = -\frac{nA}{r^{n+1}} + \frac{mB}{r^{m+1}}. \quad (7)$$

Therefore, if under the action of the same stress, the stretching distance between atoms is greater than the compression distance [66]. The stretching effect (the distance between atoms is stretched) is more obvious than the compression effect (the distance between atoms is compressed) of one dislocation in crystal. This is called dislocation

stretching and compression asymmetry.

In the untreated samples, there was residual compressive stress in the original crystals. The smaller the distance between the two atoms was the more sensitive the repulsive force was [66]. Thus, in crystals with initial residual compressive stress, the compression effect produced by dislocations would be inhibited, leading to the strengthening of the dislocation stretching and compression asymmetry. It can be concluded that the dislocation stretching and compression asymmetry generated by an edge dislocation was equivalent to effectively increasing the lattice spacing in the region where the dislocation is located.

There are few dislocations in the untreated samples [67]. The dislocation stretching and compression asymmetry were only local which was not sufficient to influence the residual compressive stress magnitude. But many uniformly distributed dislocations were generated by multiplication after the coupled electromagnetic treatment. There was a large amount enhanced dislocation stretching and compressive asymmetry in most of the region of the crystal, which reduced the residual stress.

6. Conclusions

Based on the new studies on the pulsed magnetic treatment (PMT) and coupled electromagnetic treatment (ECT) of the machining cutters and their effects on the residual stress reductions in the cutting tools the following conclusions are drawn:

Treating the cutting tools by both PMT and ECT methods would lead to the changes of the microstructure of the tools, in this case, P10 carbide tools. Compared with the

untreated P10 carbide tools, after the PMT, dislocation multiplications occurred in the WC phase and the TiC phase, but in limited quantities. However, after the ECT, the dislocations in both WC phase and TiC phase showed characteristics with multiple quantities and wide distributions, and appeared as networks.

More details on the changes of the microstructures in the cutting tools and their interactions were developed through the numerical simulations conducted using COMSOL Multiphysics software. It was shown that during the PMT, there was only the linear magnetostriction effect observed, and the deformations of the P10 carbide tools were gentle. However, during the ECT, there was not only the linear magnetostriction effect but also the Weidemann effect with torsional strains.

The study further revealed that dislocation interactions after the PMT could reduce the lattice distortion at a lower level (mutual attraction and non-mutual attraction), while the dislocation interactions after the ECT could reduce lattice distortions at a higher level (steady state and metastable state). The interactions between the dislocations could effectively reduce the lattice distortions in the region having severe dislocation deformations, which reduced destructiveness of the dislocations. As the dislocation distribution became more uniform, the residual stresses could be effectively reduced by large amounts of evenly enhanced dislocation stretching and compression asymmetry.

Combined experiment and numerical study confirmed that both PMT and ECT methods could all effectively reduce residual stresses of the cutting tools studied. Compared with the PMT, the stresses induced in the tools treated by the ECT were

obviously higher and the directions changed constantly, which made the dislocation multiplications more obvious, and there also existed a stress mutation phenomenon during the ECT. Generally, there was approximately 30% reduction of residual stresses in the cutting tools treated by the pulsed magnetic field method and 65% reduction by the coupled electromagnetic field method.

The results obtained through this study have clearly bridged gaps in developing detailed understandings of the mechanisms of residual stress reductions induced by the external fields and correlations between the microstructural changes and the stress-strain states in the cutting tools. The results can be used as a process design and quality control guidance for treating the cutting tools by both PMT and ECT methods and hence, could help to promote applications of these low-cost but effective tool-treatment techniques more widely.

Acknowledgements

The authors wish to acknowledge the financial support by the National Natural Science Foundation of China (No. 51705348), the Sichuan Science and Technology Program (No. 2021ZHCG0009), and the Special Fund for Strategic Cooperation between Yibin City and Sichuan University (2019CDYB-6). We appreciate Wang Hui from the Analytical and Testing Center of Sichuan University for her help with BSE characterization, and the Sinoma Institute of Materials Research (Guang Zhou) Co., Ltd. for the TEM/HRTEM test.

References

[1] Ghani JA, Choudhury IA, Masjuki HH. Performance of P10 TiN coated carbide tools when end milling AISI H13 tool steel at high cutting speed. J Mater Process Technol 2004;153–154:1062–6. https://doi.org/10.1016/j.jmatprotec.2004.04.353.

[2] Niu Q, An Q, Chen M, Liu G, Zhang Y. Experimental study on the performance of WC-Co inserts in turning 4Cr13 die steel. Key Eng Mater 2010;443:256–61. https://doi.org/10.4028/www.scientific.net/KEM.443.256.

[3] Obikawa T, Ohno T, Yamaguchi M, Maetani T, Unami S, Ozaki Y. Wear Characteristics of Cutting Tools in Turning of Sintered Steel under Different Lubrication Conditions. Key Eng Mater 2012;523–524:13–8. https://doi.org/10.4028/www.scientific.net/KEM.523-524.13.

[4] Akram S, Babutskyi A, Chrysanthou A, Montalvão D, Pizurova N. Effect of Alternating Magnetic Field on the Fatigue Behaviour of EN8 Steel and 2014-T6 Aluminium Alloy. Met 2019;9. https://doi.org/10.3390/met9090984.

[5] Rech J, Kusiak A, Battaglia JL. Tribological and thermal functions of cutting tool coatings. Surf Coatings Technol 2004;186:364–71. https://doi.org/10.1016/j.surfcoat.2003.11.027.

[6] Liu J, Han R, Zhang L, Guo H. Study on lubricating characteristic and tool wear with water vapor as coolant and lubricant in green cutting. Wear 2007;262:442–52. https://doi.org/10.1016/j.wear.2006.06.014.

[7] Yuan M, Wang J, Wang L, Zhong F, Huang K, Tian Y. Electromagnetic coupling field strengthening of WC-TiC-Co cermet tools. Ceram Int 2021;47:3747–59. https://doi.org/10.1016/j.ceramint.2020.09.232.

[8] Yuan M, Wang J, Wang M, Huang K, Wang L, Tian Y. Enhanced carbide tool life by the electromagnetic coupling field for sustainable manufacturing. Int J Adv Manuf Technol 2020;108:3905–14. https://doi.org/10.1007/s00170-020-05612-3.

[9] Gu Q, Huang X, Xi J, Gao Z. The Influence of Magnetic Field on Fatigue and Mechanical Properties of a 35CrMo Steel. Met 2021;11. https://doi.org/10.3390/met11040542.

[10] Jia Y, Hou J, Wang H, Le Q, Lan Q, Chen X, et al. Effects of an oscillation electromagnetic field on grain refinement and Al8Mn5 phase formation during direct-chill casting of AZ31B magnesium alloy. J Mater Process Technol 2020;278:116542. https://doi.org/10.1016/j.jmatprotec.2019.116542.

[11] Lan Q, Cheng C, Zhang J, Guo R, Le Q. The relationship between the thermoelectric power and resultant solidification microstructures of Al-Si melt under electromagnetic field. Mater Chem Phys 2019;231:203–15. https://doi.org/10.1016/j.matchemphys.2019.04.021.

[12] Jia Y, Wang H, Le Q. Transient coupling simulation of multi-physical field during pulse electromagnetic direct-chill casting of AZ80 magnesium alloy. Int J Heat Mass Transf 2019;143:118524. https://doi.org/10.1016/j.ijheatmasstransfer.2019.118524.

[13] Lan Q, Le Q, Guo R, Zhang J. Effects of melt temperature on the magnetic treated refinement of eutectic and primary phases in Al-Fe binary alloy melt by measuring

thermopower. J Cryst Growth 2020;542:125653. https://doi.org/10.1016/j.jcrysgro.2020.125653.

[14] Yang C, Xu W, Guo B, Shan D, Zhang J. Healing of Fatigue Crack in 1045 Steel by Using Eddy Current Treatment. Materials (Basel) 2016;9:641. https://doi.org/10.3390/ma9080641.

[15] Yang C, Xu W, Chen Y, Guo B, Shan D. Restoration of fatigue damage in steel tube by eddy current treatment. Int J Fatigue 2019;124:422–34. https://doi.org/10.1016/j.ijfatigue.2019.03.012.

[16] Zhang H, Wang X, Ma Y, Gu X, Lu J, Wang K, et al. Formability and mechanism of pulsed current pretreatment–assisted laser impact microforming. Int J Adv Manuf Technol 2021;114:1011–29. https://doi.org/10.1007/s00170-021-06964-0.

[17] Chen K, Zhan L, Xu Y, Liu Y. Effect of pulsed current density on creep-aging behavior and microstructure of AA7150 aluminum alloy. J Mater Res Technol 2020;9:15433–41. https://doi.org/10.1016/j.jmrt.2020.10.100.

[18] Huo K, Zhou J, Dai F, Xu J. Particle distribution and microstructure of IN718/WC composite coating fabricated by electromagnetic compound field-assisted laser cladding. Appl Surf Sci 2021;545:149078. https://doi.org/10.1016/j.apsusc.2021.149078.

[19] Sun Q, Hua L. Micro texture of titanium alloys excited nonlinearly by electromagnetic pulse. Scr Mater 2021;200:113828. https://doi.org/10.1016/j.scriptamat.2021.113828.

[20] Liu J, Wei C, Yang G, Wang L, Wang L, Wu X, et al. A Novel Combined Electromagnetic Treatment on Cemented Carbides for Improved Milling and Mechanical Performances. Metall Mater Trans A 2018;49:4798–808. https://doi.org/10.1007/s11661-018-4740-y.

[21] Su C, Liu D, Tang S, Li P, Qiu X. Finite Element Analysis of Surface Residual Stress in Functionally Gradient Cemented Carbide Tool. High Temp Mater Process 2018;37:233–43. https://doi.org/doi:10.1515/htmp-2016-0085.

[22] Krawitz A, Drake E. Residual stresses in cemented carbides - An overview. Int J Refract Met Hard Mater 2015;49:27–35. https://doi.org/10.1016/j.ijrmhm.2014.07.018.

[23] Klamecki BE. Residual stress reduction by pulsed magnetic treatment. J Mater Process Technol 2003;141:385–94. https://doi.org/10.1016/S0924-0136(03)00387-X.

[24] Wu S, Zhao H, Lu A, Fang H, Tang F. A micro-mechanism model of residual stress reduction by low frequency alternating magnetic field treatment. J Mater Process Technol 2003;132:198–202. https://doi.org/10.1016/S0924-0136(02)00915-9.

[25] Tang F, Lu AL, Fang HZ, Mei JF. Effect of magnetic treatment on magnetostrictive behaviour of HT70 steel. Mater Sci Eng A 1998;248:98–100. https://doi.org/10.1016/s0921-5093(98)00512-7.

[26] Lin J, Zhao H, Cai Z, Lei Y. Study on the relationship between magneto-vibration and residual stress in steel materials. Jinshu Xuebao/Acta Metall Sin 2008;44:451–6. https://doi.org/10.3321/j.issn:0412-1961.2008.04.013.

[27] Zhang X, Zhao Q, Cai Z, Pan J. Effects of Magnetic Field on the Residual Stress and Structural Defects of Ti-6Al-4V. Met 2020;10. https://doi.org/10.3390/met10010141.

[28] Yan M, Wang C, Luo T, Li Y, Feng X, Huang Q, et al. Effect of Pulsed Magnetic Field on the Residual Stress of Rolled Magnium Alloy AZ31 Sheet. Acta Metall Sin (English Lett 2021;34:45–53. https://doi.org/10.1007/s40195-020-01109-w.

[29] Shao Q, Wang G, Wang H, Xing Z, Fang C, Cao Q. Improvement in uniformity of alloy steel by pulsed magnetic field treatment. Mater Sci Eng A 2021;799:140143. https://doi.org/10.1016/j.msea.2020.140143.

[30] Shao Q, Kang J, Xing Z, Wang H, Huang Y, Ma G, et al. Effect of pulsed magnetic field treatment on the residual stress of 20Cr2Ni4A steel. J Magn Magn Mater 2019;476:218–24. https://doi.org/10.1016/j.jmmm.2018.12.105.

[31] Hou M, Li K, Li X, Zhang X, Rui S, Wu Y, et al. Effects of Pulsed Magnetic Fields of Different Intensities on Dislocation Density, Residual Stress, and Hardness of Cr4Mo4V Steel. Cryst 2020;10. https://doi.org/10.3390/cryst10020115.

[32] Cai zhipeng, Huang X. Residual stress reduction by combined treatment of pulsed magnetic field and pulsed current. Mater Sci Eng A 2011;528:6287–92. https://doi.org/10.1016/j.msea.2011.04.078.

[33] Cai Z, Duan X, Lin J, Zhao H. Magnetostriction varieties and stress relief caused by pulsed magnetic field. Front Mech Eng 2011;6:354. https://doi.org/10.1007/s11465-011-0123-4.

[34] Rong Y, Xu J, Lei T, Huang Y, Shao X, Wang C. Magnetism aided mitigation of deformation and residual stress in dissimilar joint 316L with EH36. J Mater Process Technol 2018;259:23–32. https://doi.org/10.1016/j.jmatprotec.2018.04.022.

[35] Hu B, Liu Y, Yu R. Numerical simulation on magnetic–mechanical behaviors of 304 austenite stainless steel. Meas J Int Meas Confed 2019;151:107185. https://doi.org/10.1016/j.measurement.2019.107185.

[36] Zhao J, Cheng Y, Han K, Zhang X, Xu Z, Zhai Q. Numerical and experimental studies of surface-pulsed magneto-oscillation on solidification. J Mater Process Technol 2016;229:286–93. https://doi.org/10.1016/j.jmatprotec.2015.09.027.

[37] Yu H, Zheng Q, Wang S, Wang Y. The deformation mechanism of circular hole flanging by magnetic pulse forming. J Mater Process Technol 2018;257:54–64. https://doi.org/10.1016/j.jmatprotec.2018.02.022.

[38] Li B, Yang J, Shu L, Li P, Wu H. Three-Dimensional Model of Magnetostrictive Force Sensor Considering Stress Coupling and Experimental Research. Xitong Fangzhen Xuebao / J Syst Simul 2018;30:3671–80. https://doi.org/10.16182/j.issn1004731x.joss.201810010.

[39] Seo H young, Shim IB. Magnetocapacitance of magnetically strained multilayered thin films. J Magn Magn Mater 2019;481:136–9. https://doi.org/10.1016/j.jmmm.2019.03.012.

[40] Zubarev A, Chirikov D, Stepanov G, Borin D. Hysteresis of ferrogels magnetostriction. J Magn Magn Mater 2017;431:120–2. https://doi.org/10.1016/j.jmmm.2016.11.069.

[41] Zubarev A, Chirikov D, Stepanov G, Borin D, Lopez-Lopez MT. On the theory of hysteretic magnetostriction of soft ferrogels. Phys A Stat Mech Its Appl 2018;498:86–95. https://doi.org/10.1016/j.physa.2017.12.136.

[42] Wang C, Yu D, Niu Z, Zhou W, Chen G, Li Z, et al. The role of pyramidal ⟨c + a⟩ dislocations in the grain refinement mechanism in Ti-6Al-4V alloy processed by severe plastic deformation. Acta Mater 2020;200:101–15. https://doi.org/10.1016/j.actamat.2020.08.076.

[43] Cullity B. D., Graham CD. Introduction to magnetic materials. Mater Today 2009;12:45.

https://doi.org/10.1016/s1369-7021(09)70091-4.

[44] Wang B, Li Y, Xie X, Huang W, Weng L, Zhang C. The output voltage model and experiment of magnetostrictive displacement sensor based on Weidemann effect. AIP Adv 2018;8:056611. https://doi.org/10.1063/1.5006418.

[45] Deng C, Kang Y, Ye B, Wang Z, Zhao X, Huang F. Characterization and control of the magnetic diffusion effect in a magnetostrictive position sensor. Meas Sci Technol 2014;25:055008. https://doi.org/10.1088/0957-0233/25/5/055008.

[46] Deng C, Kang Y, Li E, Zhang Y, Cheng J, Ge T. A new model of the signal generation mechanism on magnetostrictive position sensor. Meas J Int Meas Confed 2014;47:591–7. https://doi.org/10.1016/j.measurement.2013.09.021.

[47] Nabarro FRN. Dislocations in a simple cubic lattice. Proc Phys Soc 1947;59:256–72. https://doi.org/10.1088/0959-5309/59/2/309.

[48] Lu G, Kioussis N, Bulatov V V, Kaxiras E. Generalized-stacking-fault energy surface and dislocation properties of aluminum. Phys Rev B 2000;62:3099–108. https://doi.org/10.1103/PhysRevB.62.3099.

[49] Lu G, Kioussis N, Bulatov V V, Kaxiras E. The Peierls-Nabarro model revisited. Philos Mag Lett 2000;80:675–82. https://doi.org/https://doi.org/10.1080/09500830050143778.

[50] Xiang S, Zhang X. Dislocation structure evolution under electroplastic effect. Mater Sci Eng A 2019;761:138026. https://doi.org/10.1016/j.msea.2019.138026.

[51] Shimokawa T, Kitada S. Dislocation multiplication from the frankread source in atomic models. Mater Trans 2014;55:58–63. https://doi.org/10.2320/matertrans.MA201319.

[52] Schulz K, Dickel D, Schmitt S, Sandfeld S, Weygand D, Gumbsch P. Analysis of dislocation pile-ups using a dislocation-based continuum theory. Model Simul Mater Sci Eng 2014;22:025008. https://doi.org/10.1088/0965-0393/22/2/025008.

[53] Sudmanns M, Gumbsch P, Schulz K. Plastic flow and dislocation strengthening in a dislocation density based formulation of plasticity. Comput Mater Sci 2018;151:317–27. https://doi.org/https://doi.org/10.1016/j.commatsci.2018.04.065.

[54] He C, Li X, Liu Y, Wang C, Zhang H, Li L, et al. Localized dislocation interactions within slip bands and crack initiation in Mg-10Gd-3Y-0.3Zr alloy. Int J Fatigue 2021;150:106302. https://doi.org/10.1016/j.ijfatigue.2021.106302.

[55] Hull D, Bacon DJ. Introduction to Dislocations. Mater Today 2011;14:502. https://doi.org/10.1016/s1369-7021(11)70217-6.

[56] Wolf D. A broken-bond model for grain boundaries in face-centered cubic metals. J Appl Phys 1990;68:3221–36. https://doi.org/10.1063/1.346373.

[57] Schouwenaars R. Self-energy, line tension and bow-out of grain boundary dislocation sources. Int J Plast 2020;133:102802. https://doi.org/10.1016/j.ijplas.2020.102802.

[58] Schouwenaars R, Seefeldt M, Van Houtte P. The stress field of an array of parallel dislocation pile-ups: Implications for grain boundary hardening and excess dislocation distributions. Acta Mater 2010;58:4344–53. https://doi.org/10.1016/j.actamat.2010.04.026.

[59] Qi K-W, Zhao Y-H, Guo H-J, Tian X-L, Hou H. Phase field crystal simulation of the effect of temperature on low-angle symmetric tilt grain boundary dislocation motion. Wuli Xuebao/Acta Phys Sin 2019;68. https://doi.org/10.7498/aps.68.20190051.

[60] Shi LT, Chaudhari P. Computer Simulation of Dislocationlike Motion in a Lennard-

Jones Amorphous Solid. Phys Rev Lett 1983;51:1581–3. https://doi.org/10.1103/PhysRevLett.51.1581.

[61] Shi LT. Introduction and propagation of screw-dislocation-like defects in an amorphous Lennard-Jones solid. Mater Chem Phys 1993;36:68–76. https://doi.org/10.1016/0254-0584(93)90009-B.

[62] Li K, Fu X song, Li R dong, Zhou W long, Li Z qiang. A mechanism study on characteristic curve of residual stress field in Ti-6Al-4V induced by wet peening treatment. Mater Des 2015;86:761–4. https://doi.org/10.1016/j.matdes.2015.07.117.

[63] Dong L, Schnitker J, Smith RW, Srolovitz DJ. Stress relaxation and misfit dislocation nucleation in the growth of misfitting films: A molecular dynamics simulation study. J Appl Phys 1998;83:217–27. https://doi.org/10.1063/1.366676.

[64] Caccamo C. Integral equation theory description of phase equilibria in classical fluids. Phys Rep 1996;274:1–105. https://doi.org/10.1016/0370-1573(96)00011-7.

[65] Lim TC. A functionally flexible interatomic energy function based on classical potentials. Chem Phys 2005;320:54–8. https://doi.org/10.1016/j.chemphys.2005.07.002.

[66] Moradi A, Heidari A, Amini K, Aghadavoudi F, Abedinzadeh R. Molecular modeling of Ti-6Al-4V alloy shot peening: the effects of diameter and velocity of shot particles and force field on mechanical properties and residual stress. Model Simul Mater Sci Eng 2021;29:065001. https://doi.org/10.1088/1361-651X/ac03a3.

[67] Ma L, Liang Z, Wang X, Zhao W, Jiao L, Liu Z. Influence of pulsed magnetic treatment on microstructures and mechanical properties of M42 high speed steel tool. Jinshu Xuebao/Acta Metall Sin 2015;51:307–14. https://doi.org/10.11900/0412.1961.2014.00295.